Three tidal turbines in interaction: An experimental study of turbulence intensity effects on wakes and turbine performance

Benoît Gaurier, Clément Carlier, Grégory Germain, Grégory Pinon, Elie Rivoalen

Three tidal turbines in interaction: An experimental study of turbulence intensity effects on wakes and turbine performance

Benoît Gaurier, Clément Carlier, Grégory Germain, Grégory Pinon, Elie Rivoalen

Three tidal turbines in interaction: An experimental study of turbulence intensity effects on wakes and turbine performance

Benoît Gaurier [a], Clément Carlier [b, a], Grégory Germain [a], Grégory Pinon [b, *], Elie Rivoalen [c, b]

[a] IFREMER, Marine Structures Laboratory, 150 Quai Gambetta, 62 200 Boulogne-sur-mer, France
[b] Laboratoire Ondes et Milieux Complexes, Normandie Univ, UNIHAVRE, CNRS, LOMC, 76 600 Le Havre, France
[c] Laboratoire de Mécanique de Normandie, Normandie Univ, INSA Rouen, LMN, 76 000 Rouen, France

ARTICLE INFO

Article history:
Received 29 January 2019
Received in revised form
27 September 2019
Accepted 3 October 2019
Available online 18 October 2019

Keywords:
Marine current turbine
Performance
Wake
Turbulence
Array interaction
Experiment

ABSTRACT

The development of marine current turbine arrays depends on the understanding of the interaction effects that exist between turbines in close proximity. Moreover, the ambient turbulence intensity also plays a major role in the behaviour of tidal turbines. Thus it is necessary to take ambient turbulence into account when studying interaction effects between several turbines. In order to highlight these interaction effects, experiments have been carried out in the IFREMER flume tank. These experiments focus on interactions between three horizontal axis turbines. This paper presents the experimental results obtained for three configurations with two ambient turbulence intensity rates.

The results are presented in terms of turbine wakes and performance. The wake characterisation presents complex features for the three configurations and the lowest ambient turbulence rate: upstream turbines wakes are still present at the location of the downstream turbine and their wakes can interact or merge, depending on the tested configurations. On the contrary, for the highest turbulence rate, the downstream turbine wake is not affected in his shape by the two upstream ones which are not visible any more. In fact, as already observed in the previous studies of Mycek et al. [1, 2], the wake shape rapidly spreads out in the stream-wise direction behind the turbines. However, the velocity deficit and the turbulence intensity are higher for the downstream turbine comparing to the upstream ones. In terms of performance, one tested case presents an increase of the downstream turbine power production: when this turbine is exactly in the centre of the two upstream turbines and for the lowest turbulence rate only. A small misalignment of the layout axis with respect to the tidal current may result in a decrease of performance at the end. An analysis of the power spectral density functions of the downstream turbine torque and thrust shows that no signature of the upstream turbines can be found in these answers. Furthermore, the same spectral analysis carried out on the velocity measurements shows no signature of the upstream turbines either, from 3 diameters distance. This result is noticeable for the highest and the lowest tested turbulence cases and whatever the turbines configuration is.

1. Introduction

In the past recent years, tidal energy developments have made great steps towards the development of tidal farms. In the northern part of the United Kingdom, the first phase of the Meygen project started in 2016 with a final goal of four 1.5 *MW* tidal turbines deployed between the Stroma Islands and the Scottish mainland. But several other projects of farms are flourishing in Europe or around the world. These deployments are very encouraging for the scientific community as many topics of research are going to become real issues. Among these topics of research, one can cite interaction effects that will inevitably become true in such arrays. However, upstream flow ambient turbulence influence is also of major concern. And of course, in such real configurations, these two phenomena are combined.

So far as interaction effects are concerned, several authors already worked on array configurations [3–6]. More recently,

* Corresponding author.
E-mail addresses: benoit.gaurier@ifremer.fr (B. Gaurier), carlier.clement@gmail.com (C. Carlier), gregory.germain@ifremer.fr (G. Germain), gregory.pinon@univ-lehavre.fr (G. Pinon), elie.rivoalen@insa-rouen.fr (E. Rivoalen).

https://doi.org/10.1016/j.renene.2019.10.006

Stallard et al. and Nuernberg et al. performed experiments on interacting turbines [7,8] and this paper is based on the previous experiments performed by Kervella et al. [9]. The objective of the present study is first to complete this previous piece of work and also to favour comparisons with numerical results. A work of Chruchfield et al. [10] presented large LES computations of array containing up to 5 turbines. Finally, Malki et al. [11] or O'Doherty et al. [12] numerically studied such configurations with 3 interacting turbines. The geometrical configuration of the presented trials is very similar to the configuration used for these numerical computations.

Moreover, recent studies have shown that the ambient turbulence in the upstream flow plays a decisive role in the behaviour of horizontal axis marine current turbines. First of all, Blackmore et al. demonstrated in Refs. [13,14] that the increase of turbulence rate and turbulent length scale increases the power and thrust coefficients. The same author has previously shown in Ref. [15] that the ambient turbulence has a huge impact on the thrust coefficient of the machine, using actuator disc. Durán-Medina et al. studies [16,17] have proven the existence of a strong correlation between the fluctuation of velocity due to the ambient turbulence and the fluctuation of the energy production of a turbine. Frost et al. [18] also compared power performances for tests performed at laboratory scale and *in situ*.

The results obtained by Mycek et al. in Refs. [1,2] have shown that the ambient turbulence have a significant impact on the wake of a turbine: the higher the ambient turbulence is, the faster the dissipation of the wake is. This means that the upstream flow characteristics are recovered faster for a high turbulence intensity rate. Thus, the interactions between turbines are also heavily impacted by the ambient turbulence. For example, Mycek et al. demonstrated in Ref. [2] that, for a configuration with two turbines aligned with the upstream current, the power coefficients of the downstream turbines are higher when the turbulence intensity rate is higher. It is then necessary to evaluate with precision the influence of the ambient turbulence on the turbines as well as their interaction when turbines are deployed in close proximity.

In fact, several *in situ* studies performed on different potential implementation sites have shown huge disparities of the turbulence intensity rate I_∞ between the different sites. Many other studies cover sites such as Fall of Warness (UK) [19,20], Sound of Islay (UK) [21], Puget Sound (USA) [22], Strangford Narrows (UK) [23], East River (USA) [24–26], Bay of Fundy (Ca) [27] and Ramsay Sound (UK) [41] where turbulence intensity rates between 3.2 % and 24 % were measured. Such a huge range of turbulence intensity between the different implementation sites leads to different behaviours for the marine current turbines for each site.

The present paper focuses on the interactions between three marine current turbines for two different turbulence intensity rates. Firstly, section 2 presents the general context of the study together with the experimental set-up used for the trials. Section 2.1 presents the measurements techniques and section 2.2 details the modifications made on the turbine and rotor in order to improve the quality and reliability of the obtained results, comparing to previous models used in Refs. [1,2]. Flow characteristics are presented in section 3, in order to study the wake interactions. Finally, section 4 deals with the performance assessment, either in term of power or thrust coefficients together with the standard deviations of these quantities. Conclusion and perspectives are then summarised in the last section.

2. Experiments description

2.1. Experimental set-up

The trials have been carried out in the IFREMER (French Research Institute for Exploitation of the Sea) wave and current flume tank, depicted in Fig. 1. The flume tank working section is 18 m long by 4 m wide and 2 m deep. The stream-wise flow velocity range is 0.1 to 2.2 m/s. The free stream turbulence intensity rate in the tank is $I_\infty \simeq 15$ % [16]. By means of a grid combined with a honeycomb (that acts as a flow straightener) placed at the inlet of the working section (see Fig. 1), a low turbulent intensity rate of $I_\infty \simeq 2$ % is achieved. More details about the flume tank can be found in Ref. [29].

The present study deals with the characterisation of the interaction effects between marine current turbines. Following the previous work of Mycek et al. dealing with a single turbine [1] and two interacting turbines axially aligned with the flow direction [2], this paper focuses on 3 identical turbines with diameter D in interaction.

The concerned configuration is two upstream turbines perpendicular to the upstream flow direction and a third turbine downstream, as shown on Fig. 2. In all the tested configurations, the two upstream turbines are fixed, perpendicular to the incoming flow and with a fixed lateral bypass of 1 D. In other words, the two upstream turbine centres are laterally spaced with a distance $b_1 = 2\ D$ and the third turbine is placed 4 diameters downstream of the two upstream ones ($a = 4\ D$). Only the lateral position differs: configuration 1 consists of a centred position ($b_2 = 1\ D$, black dashed line on Fig. 2), configuration 2 consists of an off-centred position ($b_2 = 0.75\ D$, red dashed line on Fig. 2) and configuration 3 consists of an even more off-centred position ($b_2 = 0.5\ D$, green dashed line on Fig. 2). All these configurations are summarised in Table 1.

The Cartesian coordinate system is considered here, with the origin $O(0,0,0)$ exactly positioned at the centre of the two upstream turbines and $\vec{e}_x$, $\vec{e}_y$ and $\vec{e}_z$ as unit vectors (Fig. 2). Lengths being made dimension-free by the rotor diameter D, let us define $a^* = a/D$, $x^* = x/D$ and $y^* = y/D$.

Two pictures of the experimental set-up are presented in Fig. 3. Each turbine model is fixed to a lengthwise I-beam by means of 3 identical masts. The I-beams are placed over the flume tank, parallel to the upstream current and at equal distances from both sides.

The position $\vec{x}$ and velocity components $\vec{u}$ are respectively denoted by (x, y, z), and (u, v, w):

$$\vec{x} = x\vec{e}_x + y\vec{e}_y + z\vec{e}_z \tag{1}$$

$$\vec{u} = u\vec{e}_x + v\vec{e}_y + w\vec{e}_z \tag{2}$$

In order to obtain the fluctuating velocities, the flow velocity field can be expressed using the Reynolds decomposition:

$$u(t) = \overline{u} + u'(t) \tag{3}$$

where $\overline{u}$ is the time average of the $\vec{e}_x$ component of $\vec{u}$, defined by:

$$\overline{u} = \frac{1}{T}\int_0^T u(t)\,dt \tag{4}$$

where $[0;T]$ is the averaging period. Thus, ($\overline{u}$, $\overline{v}$, $\overline{w}$) represents the averaged component of the velocity, while (u', v', w') represents its fluctuating part.

The flow velocity measurements are performed by means of a bi-dimensional Laser Doppler Velocimetry (LDV) system described in Refs. [1,30,31], with a measurement volume of about 0.01 mm^3. The two laser wavelengths are 488 nm and 514 nm. The distance between the probe and the measurement point is 530 mm into the water. The water of the tank is seeded with spherical particles, which have a typical size of 10 μm and are composed of silver coated glass. For the acquisition signal, the data-rate depends on

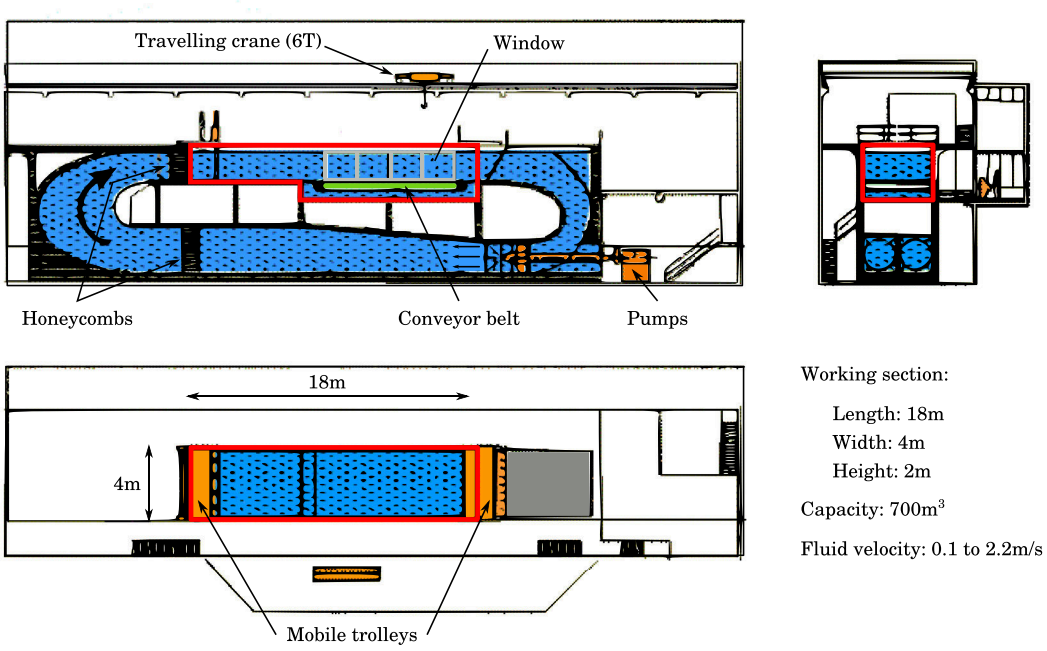

Fig. 1. IFREMER's Boulogne-sur-Mer flume tank description.

the number of particles detected by the system. The sampling frequency is irregular due to the fact that one measurement value corresponds to one detected particle.

In the following and because LDV is bi-dimensional, authors choose to use the bi-dimensional equation of the turbulence intensity rate I, which is defined by:

$$I = 100\sqrt{\frac{\frac{1}{2}\left[\sigma^2(u)+\sigma^2(v)\right]}{\overline{u}^2+\overline{v}^2}} \tag{5}$$

with $\sigma(u)$ and $\sigma(v)$ the standard deviation of the stream-wise component u and span-wise component v of the velocity. This turbulence intensity is defined relative to the local mean velocities $\overline{u}$ and $\overline{v}$.

The measurement duration on each point is $T = 180$ seconds, with an averaged data-rate between 200 *Hz* and 400 *Hz*. This duration is increased with respect to the previous study [1,2], where 100 s measurements were performed. This was justified by the need of higher convergence of various measured quantities, especially for the higher turbulence intensity level, as already discussed in Ref. [2]. The LDV measurements are performed on a grid whose detailed definition can be found in the open-data resource [32], where all the data used in this paper are given. In the lateral direction, it is important to notice that the discretization was refined in order to have a precise

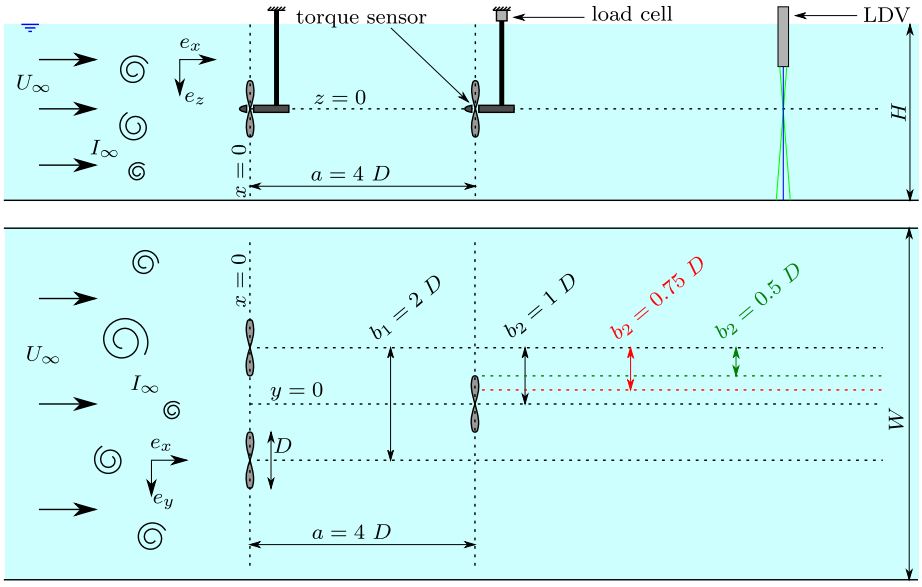

Fig. 2. Schematic side and top views of the three tested configurations with $a = 4\ D$, $b_1 = 2\ D$ and different values for $b_2 \in [1D; 0.75D; 0.5D]$ as a lateral spacing. The notation used for the geometrical configuration is taken from Mycek et al. [2] and Nuernberg & Tao [8].

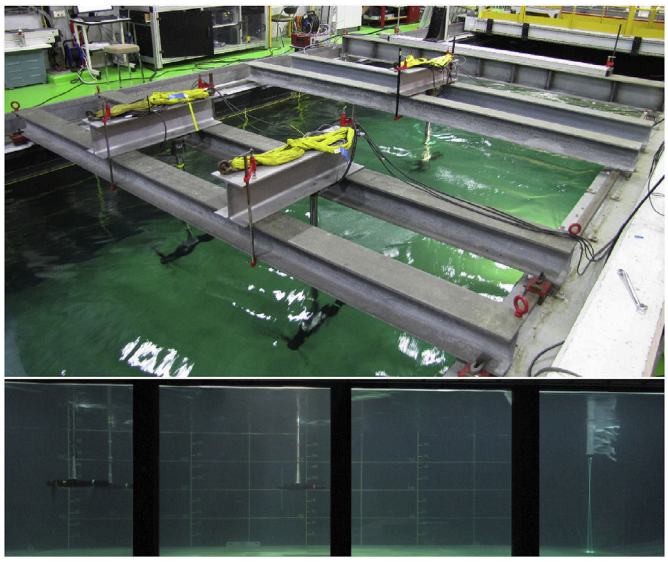

Fig. 3. Photography of the three turbines setup with $a = 4D$, $b_1 = 2D$ and $b_2 = 1D$. Top view of the assembly and side view with the 2D LDV system.

description of the velocity gradients encountered in the interaction zone.

2.2. Turbine model

The three turbines used for this work are all identical, in terms of geometry (blades, hub and nacelle) and electronics. However, in this new set of experiments, the turbines are slightly different from those used in the former studies of Mycek et al. [1,2]. Two major improvements were performed on the turbines. First, the new blades were all manufactured from the same mould in order to increase the precision and thus improve the reliability of the obtained measurements. They are made from carbon to avoid any structural deformation during the trials and have exactly the same weight. Then, the blade binding device to the shaft was improved in terms of pitch angle accuracy. With the new device, the blade pitch angle is prescribed with an accuracy of less than 0.1°. Additionally, the fixation rigidity was improved, which could be useful for the higher rotation speeds and/or incoming velocities. The rotor is still connected to a motor-gearbox assembly consisting of a gearbox, a DC motor, a ballast load and a motor speed control unit, providing an active rotor speed control. The rotation speed is now directly measured in RPM, without any conversion which also improve the accuracy of the measurement.

As a consequence, some differences were observed if compared to the previous results presented in Refs. [1,2]. In that respect, comparisons of power and thrust coefficients between the new and the former turbine are presented in sub-section 4.1 for a single turbine configuration.

As depicted on schematic 2, only the downstream turbine is instrumented. The forces and moments acting on this structure are obtained by means of a six-component load cell, which measures the three force components and the three moment components, at a 100 *Hz* sampling frequency. A torque sensor, directly fixed between the rotor and the motor, provides a more accurate measurement of the axial torque than the one given by the load cell, also at a 100 *Hz* sampling frequency.

Table 4a describes major parameters of the turbine together with a picture given in Fig. 4b. The blades profile is still designed based on a NACA 63418 and the global pitch angle is set to 0°. A complete definition of the blade geometry is given in table 3 in Ref. [1], *i.e.* the blade chord and pitch angles variations along the radius. The turbines diameter is $D = 2 \times R = 0.7\ m$. With a far upstream flow velocity $u_\infty = 0.8\ m/s$, that leads to a Reynolds number $\mathrm{Re}_\infty = 2.8 \cdot 10^5$.

The blockage ratio α is defined as the ratio between the two upstream rotors cross-sectional area $S = 2\pi R^2$ and the flume tank transverse area $A = WH$:

$$\alpha = \frac{S}{A} = \frac{2\pi R^2}{WH} \tag{6}$$

where $W = 4\ m$ and $H = 2\ m$ respectively denote the flume tank width and depth. In the present study, taking into account the two upstream rotors, the blockage ratio is $\alpha = 9.6\ \%$. This blockage ratio is doubled with respect to the previous studies [1,2]. A number of authors (*e.g.* Ref. [33]) imply that blockage corrections are necessary when blockage area ratios are higher than 5%. In addition, the blockage effect correction coefficients calculated in Ref. [34] on the same turbine model and based on [35] mainly affect the prediction of power coefficient at high rotation speeds, when thrust coefficients are high. A similar correction should have been performed again in this study. However, authors did not choose to apply any correction because the main objective of this study is to compare the turbine performance between the different configurations, all obtained with the same blockage ratio.

The Tip Speed Ratio (*TSR*) is classically defined as the ratio between the tip velocity and the far upstream flow velocity as follows:

$$TSR = \frac{\omega R}{u_\infty} \tag{7}$$

where ω is the rotor angular velocity.

The power coefficient (C_P) is given by:

$$C_P = \frac{Q\omega}{\frac{1}{2}\rho\pi R^2 u_\infty^3} \tag{8}$$

where Q denotes the turbine torque.

Finally, the thrust coefficient (C_T) is defined as follows:

Table 1
Summary of the tested configurations.

Configuration	a	b_1	b_2
config. 1	4 D	2 D	1 D
config. 2	4 D	2 D	0.75 D
config. 3	4 D	2 D	0.5 D

Description	IFREMER-LOMC
Profile	NACA 63418
Rotor Radius (R)	350 mm
Hub Radius	46 mm
Hub length	720 mm
Pitch (set angle)	0°
Studied TSR	$[0-7]$
Sense of rotation	anticlockwise
Reynolds (Re_∞)	$2.8 \cdot 10^5$ ($u_\infty = 0.8\ m/s$)

(a) Turbine model general description.

(b) Picture of the new turbine model

Fig. 4. Turbine model description.

$$C_T = \frac{T}{\frac{1}{2}\rho\pi R^2 u_\infty^2} \tag{9}$$

where T denotes the thrust applied on the device. The drag force of the hub and mast are actually not considered.

In the following, superscripts ^{up} and ^{down} added to these previous parameters stand for referencing to the upstream and downstream turbine parameters respectively.

3. Wake characterisation

3.1. Upstream velocity conditions

In the present study, two ambient turbulence conditions are considered:

1. By the use of honeycomb and grid that act as flow straightener, the turbulence intensity is relatively low to $I \simeq 2\%$.
2. Without the use of honeycomb, the natural ambient turbulence intensity of the flow is $I \simeq 15\%$.

The upstream velocity profiles are measured 1 D upstream the first turbines row ($x^* = -1$). They are shown on Fig. 5, for both turbulence rates. First of all, it is clear that the turbulence level strongly affects the standard-deviation of these measurements. This standard-deviation is higher or equal to 0.1 m/s for the highest turbulence rate whereas is stays lower or equal to 0.02 m/s for the lowest one (even lower or equal to 0.01 m/s for v_∞ component). Concerning the main stream-wise component of the velocity u_∞, a difference is noticeable in term of average velocity versus the turbulence: $\overline{u}_\infty = 0.793$ m/s for the lowest turbulence level and $\overline{u}_\infty = 0.812$ m/s for the highest one. This difference is due to the fact that the flow straightener has been removed between both cases.

The u_∞ component upstream profiles are used in the following for normalizing the measured velocity in the wake of the turbines. As already done for the lengths, a normalized velocity is introduced: $u^* = u/u_\infty$.

The upstream turbulence intensity I_∞ is depicted on Fig. 6 with the average data-rate of the LDV for the same corresponding points of the profile. As already seen with the velocity standard-deviations, the turbulence level is about 6 times higher when the flow straightener is removed, with an average value $\overline{I}_\infty = 13.5\ \%$, while it is $\overline{I}_\infty = 2.3\ \%$ for the lowest turbulent case. The first value is similar to the one obtained in the previous studies [1,2], whereas the second value is slightly lower, as some modifications were performed on the grid at the time of the experiments. The LDV average data-rate values are always between 250 and 300 Hz for every measured points, whatever the turbulence is.

In a previous study [17], Durán-Medina et al. give the inertial and integral turbulent lengths scale in the same tank and for the same flow configurations, named C_1 ($u_\infty = 0.8$ m/s and lowest turbulence rate) and C_2 ($u_\infty = 0.8$ m/s and highest turbulence rate). These parameters are given in the table B2 of this previous paper. Typically, authors found $\mathscr{L} \simeq 0.9$ m for C_1 and $\mathscr{L} \simeq 0.6$ m for C_2, concerning the integral length scale estimated from the auto-correlation method.

Finally, Table 2 summarizes these upstream main flow characteristics used in the following sections.

3.2. Wake velocity plots

Wake velocity contour plots are presented and discussed for the three turbine configurations described in Table 1 and for the previously presented flow conditions. The upstream turbines rotation speeds are the same as the downstream turbine rotation speed: $TSR^{up} = TSR^{down} = 3.5$ for every result shown in this section.

In order to encourage and facilitate comparisons of these experimental results with numerical ones, all the velocity profiles used to generate these contour plots are given in the open-data resource [32]. Due to experimental constrain, *i.e.* impossibility to deploy the LDV probe, velocity measurements are performed for $x^* \in [1.2; 11]$. Furthermore, a white zone is present on these plots between $3 < x^* < 5.2$, corresponding to the presence of the downstream turbine.

Fig. 7 presents the normalized velocity u^* for the three configurations and for both turbulence rates. Comparing these plots, it is clear that the turbulence rate has a significant effect on the velocity deficit. First, between both turbines rows, *i.e.* for $1.2 < x^* < 3$, the velocity deficit is stronger when the turbulence rate is low: $u^* \leq 0.5$ on the width of both upstream turbine diameters for the lowest turbulence rate. On the contrary, for the highest turbulence rate, the velocity deficit decreases from $u^* = 0.5$ to $u^* = 0.8$ between $x^* = 1.2$ and $x^* = 3$. However, for a given turbulence rate, no noticeable difference appears in terms of velocity, between the three tested turbines configurations, for $1.2 < x^* < 3$. Downstream the second turbine row, *i.e.* for $x^* \geq 5.2$, the velocity deficit is stronger again for the lowest turbulence rate, with large areas of about 2 D long where $u^* \leq 0.4$ (Fig. 7a). On the contrary, at the same position and for the highest turbulence rate, the smallest values are $u^* \geq 0.5$ which only appear for very small patches with a

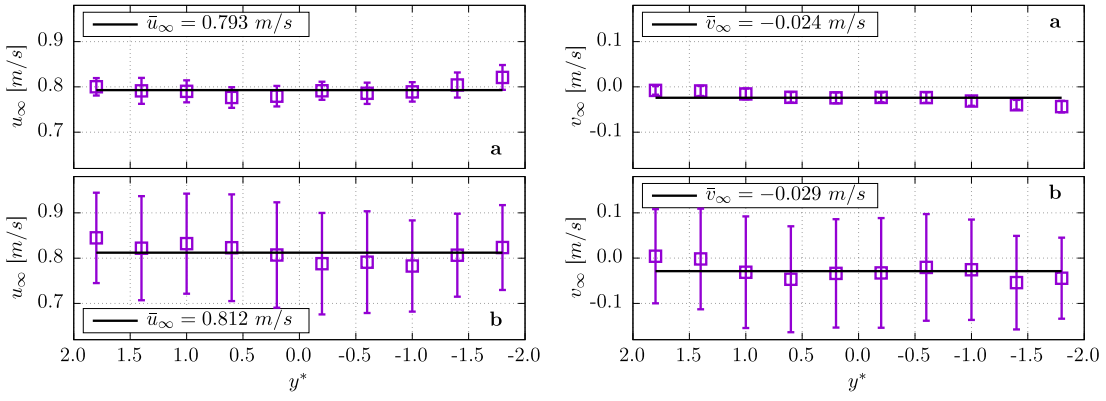

Fig. 5. Upstream u_∞ (left-hand side) and v_∞ (right-hand side) velocity profiles across the tank, for low (**a**) and high (**b**) turbulence intensity rates. Symbols □ represent the mean values, while error bars represent the corresponding standard-deviations. The dashed lines stand for the spatial average over the complete profile.

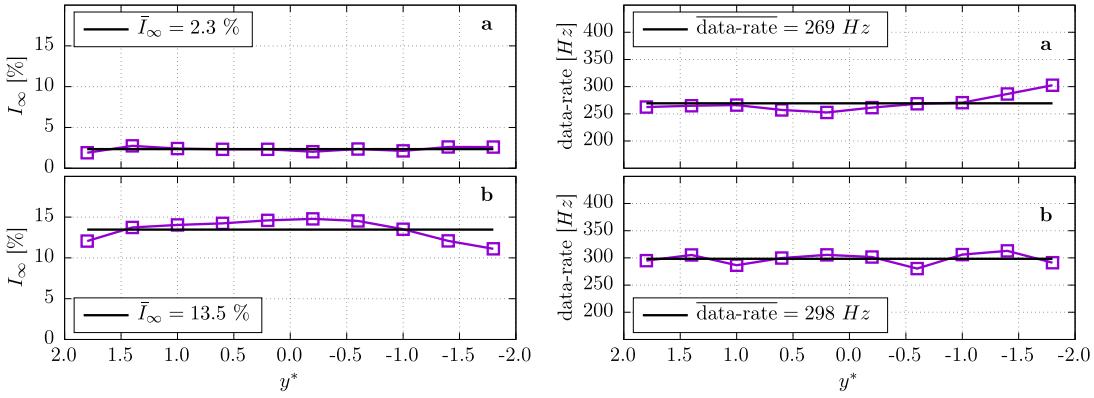

Fig. 6. Corresponding I_∞ (left-hand side) and averaged data-rate (right-hand side), for low (**a**) and high (**b**) turbulence intensity rates. The dashed line stands for the spatial average over the complete profile.

Table 2
The upstream flow characteristics, from the profile measured at $x^* = -1$

Flow case	$\bar{u}_\infty$ [m/s]	$\sigma(u_\infty)$ [m/s]	$\bar{v}_\infty$ [m/s]	$\sigma(v_\infty)$ [m/s]	I_∞ [%]
low turbulence	0.793	0.024	−0.024	0.011	2.3
high turbulence	0.812	0.107	−0.029	0.112	13.5

size shorter than 0.5 D (Fig. 7b).

As already observed for the first part of the plots, differences between the tested configurations are not really perceptible for the highest turbulence rate and for $x^* \geq 5.2$. According to these plots, the three wakes are globally the same, whatever the transverse position of the downstream turbine is (Fig. 7b). On the contrary, at the same location, wakes for the lowest turbulence rate are different (Fig. 7a). For config. 1 (top) the velocity deficit shows the three turbines wake until $x^* \simeq 6$, with the centre wake larger and stronger. From $x^* \geq 7$, a single wide wake is still visible, with stronger intensity in the middle and a width of $y^* \simeq 3$ at $x^* = 8$. For config. 2 and especially for config. 3 (bottom), two different wakes can be observed:

1. The stronger one for $y^* < 0$, where the downstream turbine wake amplifies the one coming from the same side upstream turbine and
2. The second one centred at $y^* = 1$, with a lower intensity, coming from the other side upstream turbine ($y^* > 0$).

On Fig. 8 are depicted the filled contour plots of the bi-dimensional turbulence intensity I processed with formula 5, for both ambient turbulence rates and the three tested configurations. These plots are really different between both turbulence rates. The stronger gradients are reached for the lower turbulence rate

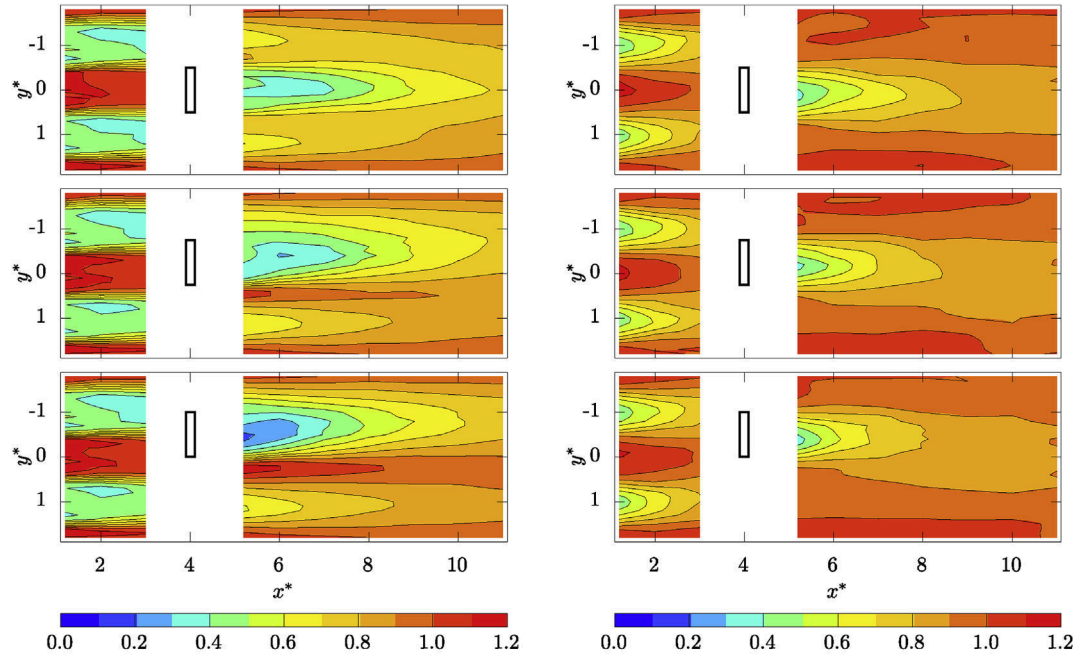

Fig. 7. Stream-wise normalized velocity $\bar{u}^*$ filled contour plots around the three turbines for configurations 1, 2 and 3 (top to bottom) and $TSR^{1;2;3} = 3.5$, for both turbulence rates. Rectangles stand for the position of the downstream turbine, where velocity measurements are impossible due to experimental constraints.

(Fig. 8a) where the tank ambient turbulence intensity is lower than 5 % and maximum values $I \geq 40$ % are noticeable in the wake of the downstream turbine, especially for config. 3. The wake organization is different between config. 1 and 3, for the lowest turbulence rate. It looks like a single wide wake for config. 1 (top) especially for $x^* \geq 8$, whereas two different wakes are clearly visible for config. 3 (bottom) with highest values for $y^* < 0$. On the contrary, turbulence wakes are quite identical for the highest turbulence rate versus configurations (Fig. 8b), in term of amplitude as well as geometrical shape.

In order to better highlight differences between cases, some profiles have been extracted and compared on Fig. 9.

For profiles measured in-between the turbine rows at $x^* = 3$, no difference appears between configurations (Fig. 9a). However, significant differences are clearly noticeable between turbulence rates. For the lowest one, there are strong gradients at $y^* = [-1.5; -0.5; 0.5; 1.5]$ corresponding to the tips of the two upstream turbines, between $u^* = 0.4$ and $u^* = 1.1$. This particular profile shows the Venturi effect in-between the first upstream turbines, with an increase of the velocity with $u^* \geq 1$ for $y^* \in [-0.4; 0.4]$. Consequently, it is of a great interest to place the second downstream turbine at the very centre, *i.e.* at $y^* = 0$, to artificially improve its performance. When the turbulence is higher, this Venturi effect disappears and $u^* = 1$ for $y^* = 0$. At the same time, the gradient is lower as well, with minimum velocity values of $u^* = 0.8$ for $y^* = [-1.0; 1.0]$.

Concerning the first profile measured just after the downstream turbine at $x^* = 5.2$ (Fig. 9b), large differences appear between configurations and turbulence rates. For the lowest turbulence case, the profile obtained for config. 1 is approximately symmetric to $y^* = 0$, with the highest velocity deficit $u^* = 0.4$ for $y^* = 0$. Positions of both the upstream turbines are still visible on this profile with a second peak in the velocity deficit $u^* \simeq 0.6$ for $y^* = [-1.2; 1.2]$. For config. 2, the maximum of the velocity deficit is still reached for $y^* = 0$ with a value slightly lower than $u^* = 0.4$, but an increase of the velocity is noticeable in parallel for $y^* = 0.5$ with value slightly higher than $u^* = 1$. For config. 3, the trend already observed for config. 2 is amplified: the maximum of the deficit appears for $y^* = -0.5$ with an extreme value $u^* = 0.2$ and a strong gradient for $y^* \in [-0.5; 0.3]$ and velocity value reaching $u^* \simeq 1.15$ for $y^* = 0.3$. For both config. 2 and 3, the position of the upstream turbine at $y^* = 1$ is observable in the velocity profile, with exactly the same values than those observed for config. 1. For the higher turbulence rate, the three profiles are quite identical in term of amplitude and shape, with a velocity deficit just lower than $u^* = 0.4$. However, a shift is observable between the configurations and the maximum of deficit appears for $y^* \simeq [0.1; -0.2; -0.4]$ respectively for config. 1, 2 and 3.

In the middle of the measured wake, *i.e.* at $x^* = 8$ (Fig. 9c) the shape of the profiles obtained for the lowest turbulence rate are globally close to those previously described, but amplitudes are reduced. The maximum of the velocity deficits are reached at $y^* = [0; -0.5; -0.75]$ with corresponding values $u^* \simeq 0.5$. The previously observed gradient is visible again for config. 2 and 3 for $y^* \in [-0.5; 0.5]$ and $y^* \in [-0.75; 0.25]$, with a maximum velocity values $u^* = 0.9$ and $u^* = 1.0$, respectively. Again, for all the three configurations, the upstream turbine located at $y^* = 1$ is still observable with a maximum velocity deficit $u^* = 0.8$ reached for $y^* \simeq 1.2$. For the highest turbulence rate, profiles show velocity deficit with small amplitudes: *e.g.* u^* is always between 0.8 and 1.0 for config. 2 and 3. Only config. 1 presents a deficit lower than 0.8 for $y^* \in [0.0; 0.5]$.

Finally, the last profiles measured at $x^* = 11$ (Fig. 9d) show quite identical curves for the lowest turbulence rate, excepted in the range $y^* \in [-0.5; 1.0]$ where differences in term of velocity amplitudes reach about 0.2. The highest deficit is measured for config. 1 at $y^* = 0$ and the maximum velocity is noticed for config. 3 at $y^* = 0.3$. On the contrary, profiles shown for the highest turbulence rate are all similar. A slight deficit is observed at the very centre of the measured area, with value $u^* \simeq 0.9$. As observed in this section,

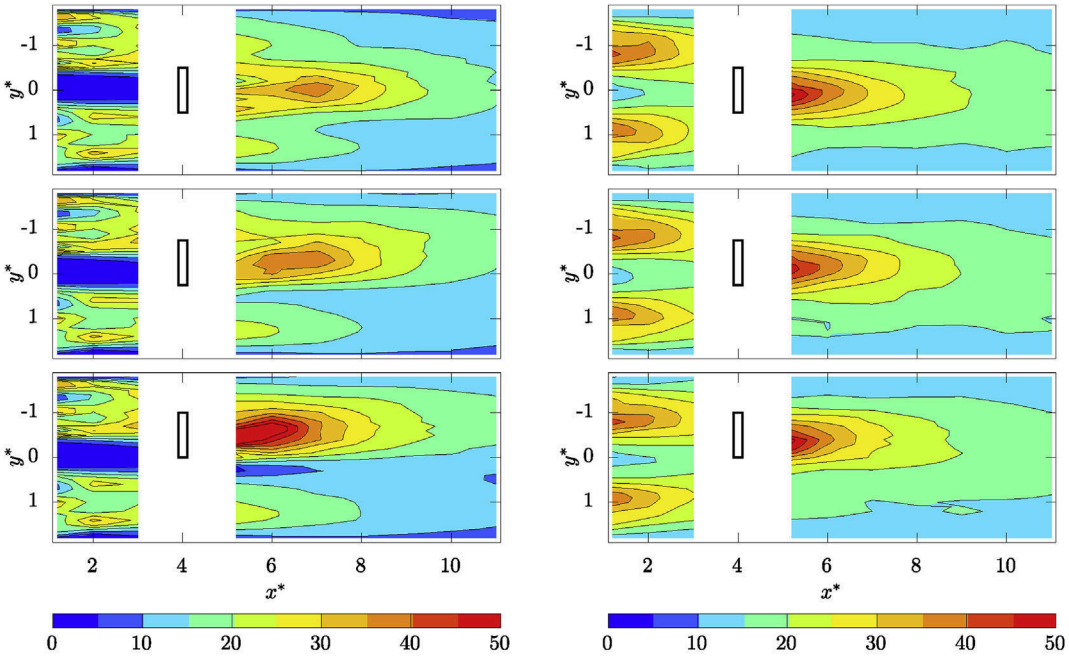

(a) I for the lowest turbulence rate

(b) I for the highest turbulence rate

Fig. 8. Turbulence intensity I filled contour plots around the three turbines for configurations 1, 2 and 3 (top to bottom) and $TSR^{up} = TSR^{down} = 3.5$, for both turbulence rates. Rectangles stand for the position of the downstream turbine, where velocity measurements are impossible due to experimental constraints.

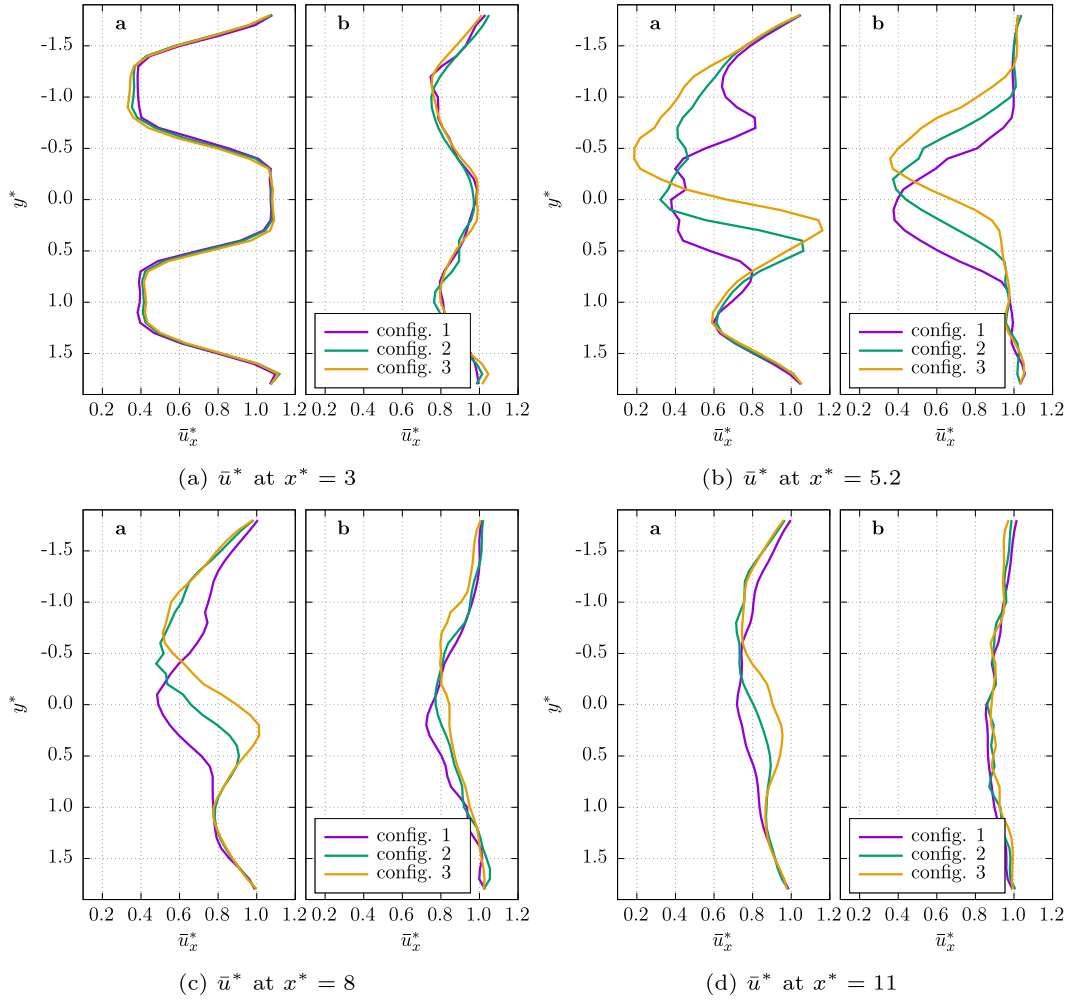

Fig. 9. Stream-wise normalized velocity $\bar{u}^*$ profiles comparisons, for the lowest (**a**) and the highest (**b**) turbulence rates.

whatever the configuration is and for the highest turbulence intensity, a rapid recovery of the wake is noticed. In term of engineering approach, this result is very interesting for turbines layout in a farm during the array development or for optimisation of turbine positioning (see for instance Ref. [36]). For the lowest turbulence intensity, interactions really occur and accurate computations of such configurations can be challenging for the scientific community.

4. Performance evaluation

As already presented in section 2.2, only the downstream turbine is instrumented in order to quantify the interaction effects in terms of C_P (power coefficient) and C_T (thrust coefficient). The acquisition duration is the same than the one used for the wake characterisation, *i.e.* $T = 180\ s$ and the sampling frequency is 100 *Hz*. In the former study of Mycek et al. [2], the turbines were aligned with the flow direction. Therefore, it was possible to evaluate a disc-integrated velocity perceived by the downstream turbine without too much experimental bias owing to the axi-symmetrical configuration. In the present configuration however, assessing such a quantity for the downstream turbine is not possible as the axi-symmetrical configuration is broken. Finally, authors chose to use the reference incoming velocities $\overline{u}_\infty$ measured along the upstream profile at $x^* = -1$, presented on Fig. 5 and given in Table 2, to process *TSR*, C_P and C_T in formula 7 to 8. During all the trials presented in the following of this section, the two front turbines were always rotating at a constant *TSR* of 3.5.

4.1. Force and torque measurements, single turbine comparisons with previous studies

As described in section 2.2, modifications regarding the blade manufacturing and the blade binding device to the shaft generate changes in the power and thrust values for the single configuration case, comparing to previous studies. The values obtained with the actual turbine are depicted on Fig. 10 and are compared to those obtained using the former one.

For the lowest turbulence rate, it can be noticed that the power coefficient curve of the actual turbine is very similar to the one of the previous work of Mycek et al. [1] except for the latter part of the curve (Fig. 10a). In fact, the present C_P curve starts decreasing from $TSR \simeq 4.5$ in the present study against $TSR \simeq 5.5$ previously. This is probably due to the improvement of the blades fixation devices.

For the thrust coefficient curve, differences can be observed (Fig. 10c). When $TSR < 3$ the thrust coefficient of the actual turbine is lower than the one obtained for the previous one. For higher *TSR* values ($TSR > 4.5$), the C_T value keeps increasing with the *TSR* for the actual turbine whereas it was stagnating for the previous studies. To some extent, this last feature could be attributed to the rigidity

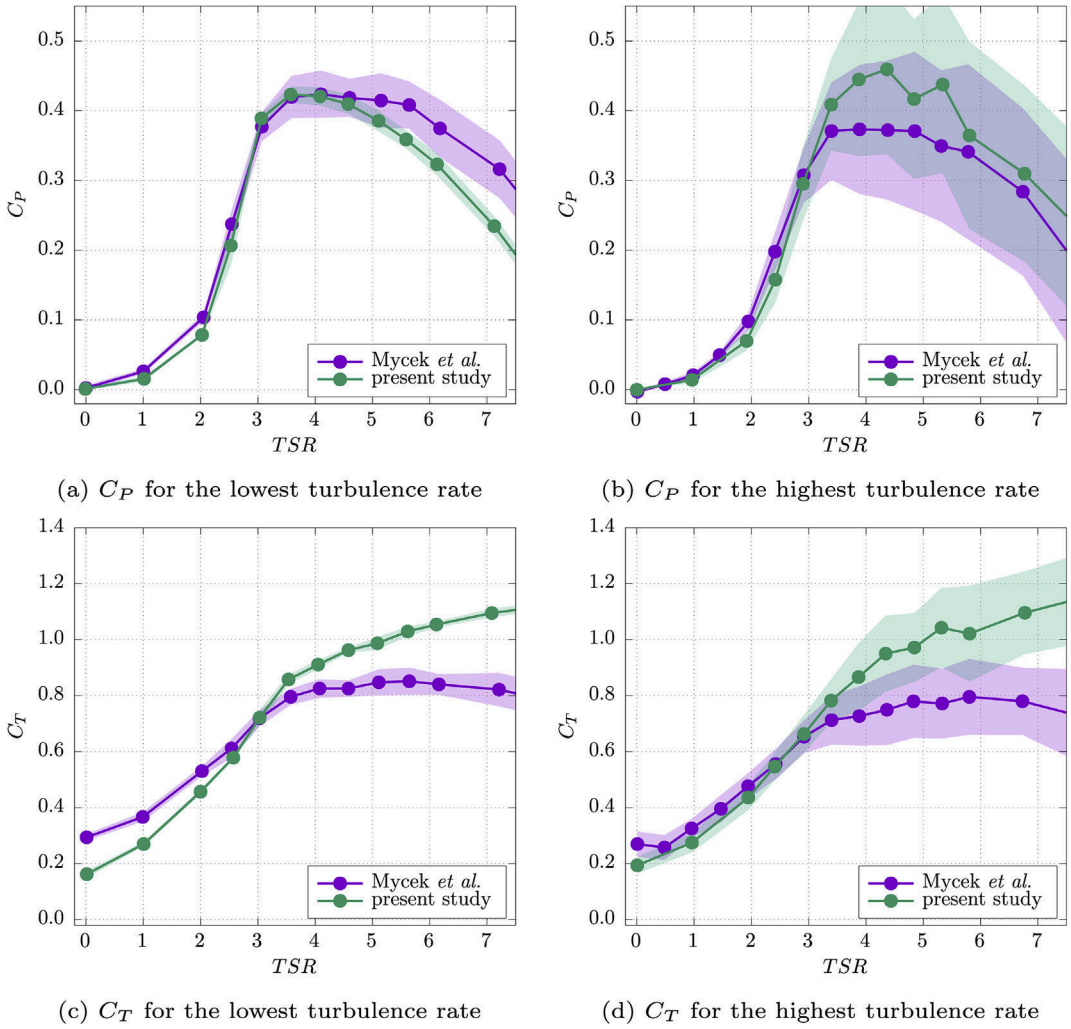

(a) C_P for the lowest turbulence rate

(b) C_P for the highest turbulence rate

(c) C_T for the lowest turbulence rate

(d) C_T for the highest turbulence rate

Fig. 10. Comparison of power and thrust coefficients between the turbine used in Mycek et al. [1,2] and the present improved turbine when used alone into the tank. Colour areas denote standard deviations of the presented quantities. (For interpretation of the references to colour in this figure legend, the reader is referred to the Web version of this article.)

improvement of blades fixation devices. In fact, small blade movements have been cancelled, so the energy losses are lower and an increased force is acting on the turbine. Conversely, this could be an argument proving that passive blade deformation or movement can increase the working range of the turbine as recently suggested by Cognet et al. [37] in the wind energy framework. This suppression of small blade movements probably also explain the lower fluctuations of C_P and C_T experienced by the actual turbine for the higher *TSR*. These values of power and thrust coefficients are the same as those measured by Gaurier et al. [34].

For the higher turbulence intensity, the actual C_P-curve is very similar to the former one, except for the peak value which is higher in the nominal working range of the turbine (Fig. 10b). Additionally, the tendency to show a plateau for the C_P-curve in Ref. [1] for $TSR \in [3;6]$ is not any more recovered for the actual turbine. Again, this tendency is explained by the rigidity improvement of blade fixation. Comparing the curves between the turbulence intensities, it can be noticed that the actual turbine shows higher C_P values for the higher turbulence rate, when the opposite was found for the former turbine. Results obtained for the thrust coefficient measured for the highest turbulence rate (Fig. 10d) are very similar to those obtained for the lowest turbulence rate.

Finally, this comparison between actual and former turbine performance coefficients leads to:

1. The plateau found in the previous study for $TSR \in [3;6]$ does not exist any more for the actual turbine and thus for both turbulence rates.
2. The thrust values are slightly higher than before, especially for the higher *TSR*.
3. The present turbine power and thrust coefficients are very close between the two different tested turbulence rates, although that the values measured for the highest one are slightly higher.

4.2. Power and thrust coefficients of the downstream turbine

In this section, the downstream turbine efficiency is evaluated in terms of power and thrust coefficients for each of the 3 configurations presented in Table 1 and for the two different upstream flow characteristics shown in Table 2. In the following, the two upstream turbines tip speed ratios are kept constant with $TSR^{up} = 3.5$.

Figs. 11 and 12 present the results for the power and thrust coefficients respectively and for the three configurations (coloured curves). The black curve shown on every plot stands for the single turbine results presented in the previous section.

A power increase is clearly observed for configuration 1 and for the lowest turbulence rate (Fig. 11a). This was anticipated owing to the velocity increase $u^* \simeq 1.1$ between the two upstream turbines $y^* \in [-0.4 : 0.4]$ at $x^* = 3$, see Fig. 9a. This increase of C_P of about 15–20% depending on the *TSR* is directly related to the velocity increase. On the contrary, the power coefficient curve for configurations 2 is exactly the same than the one for a single turbine. The curve obtained for configuration 3 is however by far lower (40%). These last observations are related to the strong velocity gradient centred for $y^* = -0.5$ observed on Fig. 9a. For configuration 2, local accelerated velocity $u^* = 1.1$ compensate the turbine swept area subjected to velocity deficit $u^* = 0.4$ of the upstream turbine wake. For configuration 3, the downstream turbine centre is exactly at $y^* = -0.5$. That means the turbine is located in the centre of the velocity gradient and blades perceive a highly sheared flow between $u^* = 0.4$ and $u^* = 1.1$ at each rotation.

This phenomenon is absolutely not reproduced for the highest turbulence rate (Fig. 11b). All the three curves show about the same amplitude, which is lower than the single turbine curve by approximately 20 %. However, a slight difference is observed between configurations with higher values for configuration 1. Again, this small difference is explained by the velocity profile perceived by the downstream turbine (see Fig. 9a), which shows u^* decreasing from 1 to 0.8 for $y^* \in [0; -0.5]$.

Following the presented power coefficient results, except for configuration 1 and for the lowest turbulence rate, these layouts should be avoided for real farm configuration and longer inter-device distance than $a = 4\ D$ should clearly be considered, whatever the ambient turbulence is.

The thrust is of major importance in term of foundation design. Thrust evaluation for a single turbine in a flow is well studied and some references can be consulted such as [1]. However, thrust modifications due to turbine interaction is not commonly evaluated even if Mycek et al. [2] evaluated the C_T modification for a downstream turbine, exactly aligned with the flow. In all the studied configurations (for different inter-device distances a), the C_T values were always lower than for the reference single configuration. The C_T curves tend to recover to the reference configuration with increasing the inter-device distance a and more rapidly for the highest turbulence rate.

For the highest ambient turbulence flow, the C_T-curves are always lower than for the reference case in the working range of *TSR* (see Fig. 12b). The difference is about 5–10% between the single turbine curve and the three configurations curves. As already observed for the power coefficient (Fig. 11b), even if the thrust measured for the three configurations is very similar, configuration 1 is slightly higher than configuration 2 and configuration 3. Again, this is directly related to the flow velocity profile measured on Fig. 9a.

For the lowest turbulence rate (Fig. 12a), the behaviour of the C_T-curves is also consistent with what was found for the C_P: an increase of about 15% for configuration 1, a smaller increase lower or equal to 10% for configuration 2 and a decrease of about 10% for configuration 3. These differences between configurations for the thrust coefficient are lower than the ones noticed for the power coefficient because the velocity gradient observed on Fig. 9a are squared and not cubed.

In term of turbine reliability, loads fluctuation are of extreme importance. Figs. 13 and 14 show that the downstream turbine standard deviation of the power and thrust coefficients are always higher than those of a single turbine.

For the lowest turbulence rate, in both cases (C_P, Fig. 13a and C_T, Fig. 14a), configuration 3 shows higher standard deviation than configuration 2, itself higher than configuration 1. This tendency results from the fact that configuration 2 and even more configuration 3 are subjected to a highly sheared flow and higher local velocity fluctuations, as already observed on the flow velocity profiles shown on Fig. 9a.

In terms of absolute values, the C_P standard deviation is at least doubled (configuration 1) or tripled (configuration 3), in the working range of *TSR*. For the thrust coefficient C_T, a large increase is observed: between three times higher for configuration 1 to approximately seven times higher for configuration 3 comparing the results of a single turbine. Another important aspect to notice is that, even for configuration 1, σ_{C_P} and σ_{C_T} increase with respect to the reference single turbine. According to the turbulence contour plot shown on Fig. 8a, this is mainly caused by the turbulence increase observed for $y^* \leq -0.5$ and $y^* \geq 0.5$, and by the strong velocity gradient observed on Fig. 9a at $y^* = [-0.5; 0.5]$, *i.e.* at the exact position of the downstream turbine blades tips.

For the higher ambient turbulence intensities (Figs. 13b and 14b), a general moderate increase of these two quantities is also observed. This increase is in fact moderate and similar whatever the configuration is. This smaller increase is explained by both the fact that the incoming velocity fluctuations are slightly higher than the ambient values and the perceived velocity profile (Fig. 9a) does not

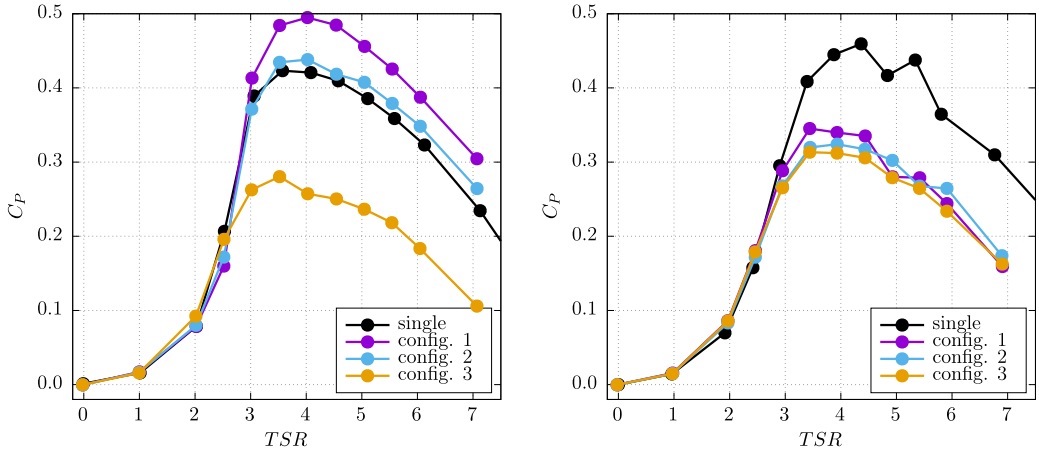

(a) lowest turbulence rate (b) highest turbulence rate

Fig. 11. Downstream turbine power coefficient C_P^{down} versus TSR^{down}, with $TSR^{up} = 3.5$, compared to C_P obtained for a single turbine.

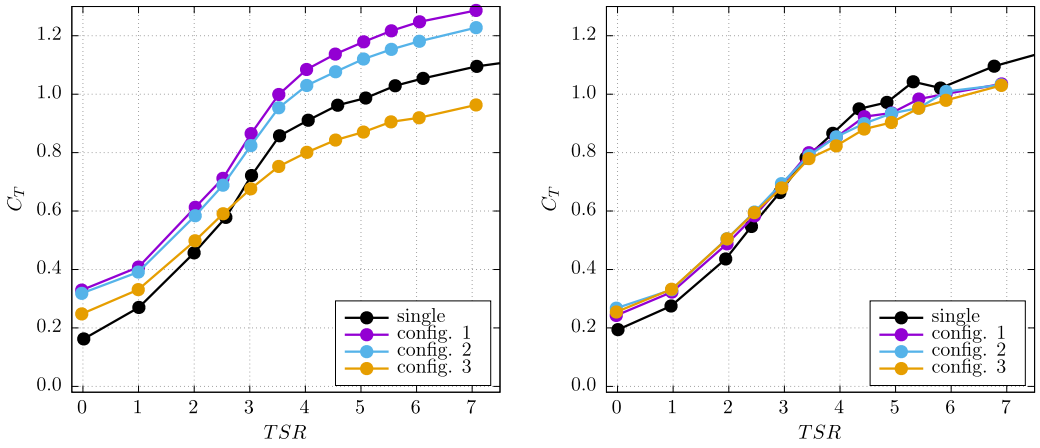

Fig. 12. Downstream turbine thrust coefficient C_T^{down} versus TSR^{down}, with $TSR^{up} = 3.5$ compared to C_T obtained for a single turbine.

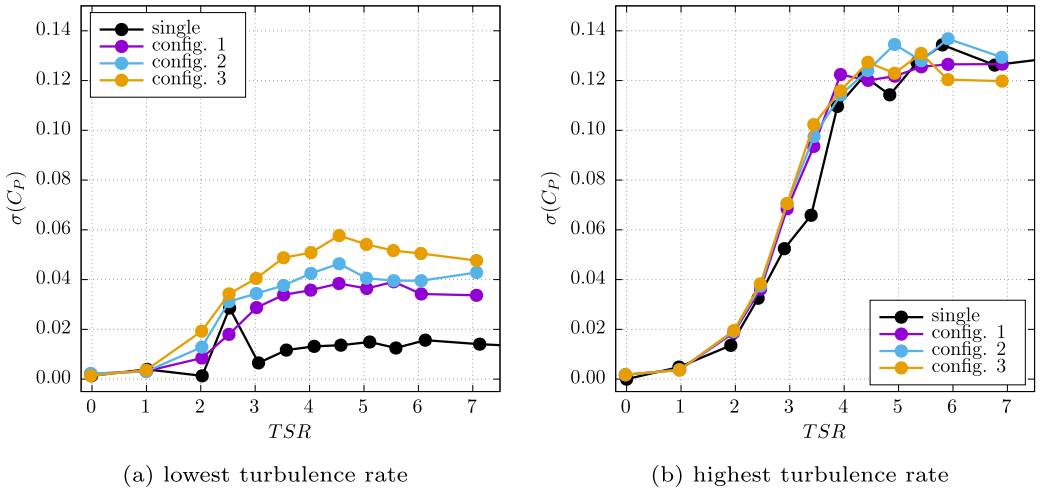

Fig. 13. Standard deviation of the downstream turbine power coefficient C_P^{down} versus TSR^{down}, with $TSR^{up} = 3.5$, compared to $\sigma(C_P)$ obtained for a single turbine.

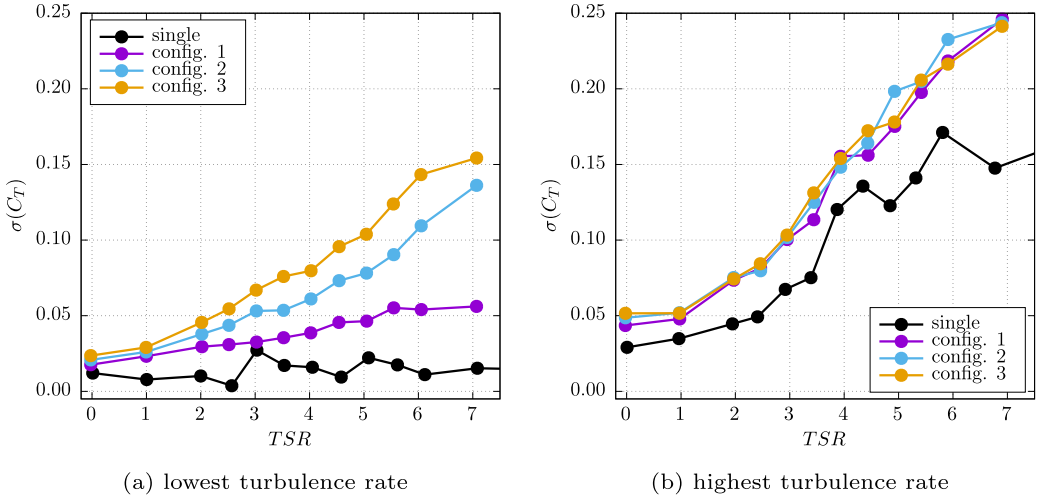

Fig. 14. Standard deviation of the downstream turbine thrust coefficient C_T^{down} versus TSR^{down}, with $TSR^{up} = 3.5$, compared to $\sigma(C_T)$ obtained for a single turbine.

show high velocity gradients. As a matter of fact, an increase of approximately 5 to 10% of the σ_{C_P} is encountered, whereas about 20 to 30% of increase is observed for the σ_{C_T}. Again, the thrust coefficient seems to be much more sensible than the power coefficient. As explained in section 2.2, the thrust is not measured directly on the turbine axis but from the top of the mast outside the water, on the contrary to the torque. This may explain the higher standard-deviation observed on this parameter which partially comes from the mast drag as well, comparing to the torque.

The following spectral analysis of the thrust and torque signals will give some interesting insights to the observed phenomena.

4.3. Power spectral density functions of the torque and thrust

In order to analyse spectral content of the torque Q^{down} and thrust T^{down}, power spectral density (PSD) functions of these two quantities are calculated for each configuration. The definition used for the power spectral density of any signal $g(t)$ is the following:

$$S_{gg} = \mathscr{F}\mathscr{T}(\gamma_g) = \mathscr{F}\mathscr{T}(g) \cdot \mathscr{F}\mathscr{T}^*(g), \tag{10}$$

where $\mathscr{F}\mathscr{T}(g)$ means the Fourier transform, $\mathscr{F}\mathscr{T}^*(g)$ its complex conjugate and γ_g the auto-correlation function of the signal $g(t)$. The present results are computed from the second part of equation (10), similarly to Durán-Medina et al. [17]. The graphics of the left (respectively right) hand side of Fig. 15 depict S_{QQ} (respectively S_{TT}) for each of the three configurations and for selected $TSR^{down} \in [0; 2; 4; 6]$. This analysis was performed directly on the fluctuating part of the torque and thrust parameters, instead of non-dimensionalised values such as C_P or C_T, in order to avoid perturbation in the signal that could come from fluctuations or oscillations of the rotational speed ω^{down}. The S_{QQ} and S_{TT} are computed over the entire acquisition length. Beforehand, the fluctuating part of the thrust and torque signals are cut into blocks of 1024 points and the Fourier transform is applied on every block. Additionally, in order to focus our attention on the interaction effects of the upstream turbines to the downstream one, all the results are presented with respect to non-dimensionalised frequency f/f^{up}, with f^{up} the upstream turbines rotation speed. As explained in section 4.2, the upstream turbine rotation speeds are constant with $TSR^{up} = 3.5$, meaning $f^{up} = 1.27\ Hz$. In the same way, f^{down} is introduced as well, corresponding to the downstream turbine rotation frequency, which differs depending on the TSR^{down} cases.

The obtained results show that the frequency f^{up}, or probably $3\ f^{up}$, cannot be observed on any of the graphics depicted on Fig. 15. On this figure, S_{QQ} function only shows a peak at $3\ f^{down}$ and, in some cases, a similar peak at f^{down}. This spectral content for the torque is very classical and similar results were obtained by Martinez et al. [38] in their recent publication for instance. Sometimes, another smaller peak at $2\ f^{down}$ can be observed: $TSR = 6.0$ for configuration 1, $TSR = 4.0$ and 6.0 for configurations 2 and 3. However, in none of these configurations a peak can be observed at $3\ f^{up}$, neither on the graphics of Fig. 15 nor in those of the other unrepresented downstream TSR (see Ref. [32]).

This result tends to prove that, even for very low ambient turbulence rate (see section 3.1), there is no spectral content of the upstream turbine that can be observed in the downstream signal, even for configurations where the upstream wake highly interact with the downstream turbine (for instance configurations 2 and 3 as presented in section 3). An additional proof is that, for $TSR = 0.0$ on each of these 3 graphics, nothing can be observed for f^{up} nor 2 or $3\ f^{up}$ and the obtained power spectral density functions S_{QQ} quite smoothly decrease for this frequency range. In terms of turbine fatigue and life cycle analysis, this results would mean that downstream turbines could be analysed individually. In other words, the inter-device distance in a farm will not have such an important effect on fatigue and reliability analysis, it would be more the surrounded or wake generated turbulence that will have. These conclusions are obtained from the 3 studied turbine layouts, but this geometrical configuration were chosen to highlight turbine interaction and are there more concentrated than in real future commercial farms. Also, this analysis is presented here based on the lowest turbulence rate, however the same results were obtained for the highest turbulence rate and the same conclusions can be drawn: there is no evidence of any spectral content at f^{up} nor 2 or $3f^{up}$ in the downstream signals.

In order to give additional informations about the upstream turbines wake influence, the power spectral density functions coming from several points in the wake in-between the turbine rows are plotted on Fig. 16 for the lowest turbulence rate. Four transverse positions are chosen $y^* = [0, -0.3, -0.5, -0.7]$, partially corresponding to the downstream turbine axis positions (configuration 1 for $y^* = 0$ and configuration 3 for $y^* = -0.5$). At the first position $x^* = 1.2$, the frequency $3\ f^{up}$ is clearly observable for $y^* = -0.5$ with harmonics 2, 3 and 4. The same frequency is visible for $y^* = -0.3$ as well, but with lower amplitude. At this later position, f^{up} can be also noticed. However, none of these frequencies are visible for $y^* = 0$ or $y^* = -0.7$. Concerning the last measured profile just in front of the downstream turbine at $x^* = 3.0$, *i.e.* 1 D upstream the turbine, no frequency is clearly detectable on every presented PSD. That means the wake activity containing the upstream turbine rotation informations seen for $y^* = [-0.3, -0.5]$ has vanished between $x^* = 1.2$ and $x^* = 3.0$. This explains why the downstream turbine PSD of torque or thrust does not contain any upstream frequency, as nothing can already be observed in the incoming velocity.

5. Conclusions and prospects

This paper presents the experimental work performed on three configurations of three tidal turbines layout. Each of these configurations has been tested for two turbulence intensity rates ($I_\infty = 2.3\%$ and $I_\infty = 13.5\%$) to emphasise the ambient turbulence influence on the obtained results. Interactions effects have been studied from wake characterisation and turbine performance. Downstream power and thrust coefficients highlight the upstream wakes effects on the downstream turbine. Load fluctuations have been quantified in terms of standard deviation of the power and thrust coefficients, and on power spectral density function of the torque and thrust forces. The use of the power spectral density function permits to investigate if a spectral signature of the upstream wake is observable in the downstream turbine behaviour. The wake and performance measurements are presented with much details in the core of the paper and all the raw materials can be obtained via the open-data resource [32].

Physically speaking, the wake characterisation presents complex features in the wake recovery for the two configurations where the downstream turbine is off-centred and for the lowest ambient turbulence rate. Wake interactions and wakes merging are observed. For this turbulence rate, the symmetric configuration shows an intense downstream turbine wake. The lateral expansion of this downstream wake is favoured with respect to the single turbine case. As a consequence, a merging of the top end of the two upstream wakes with the downstream one is encountered from $x^* = 6.0$. This feature has already been found in some previous numerical computations, *e.g.* in Ref. [39]. The generated turbulence in the downstream wake, gradually increases between the symmetrical and the more off-centred configuration. For the highest turbulence rate, the wake characterisation does not show any significant wake-turbine interactions. However, the wake recovery is

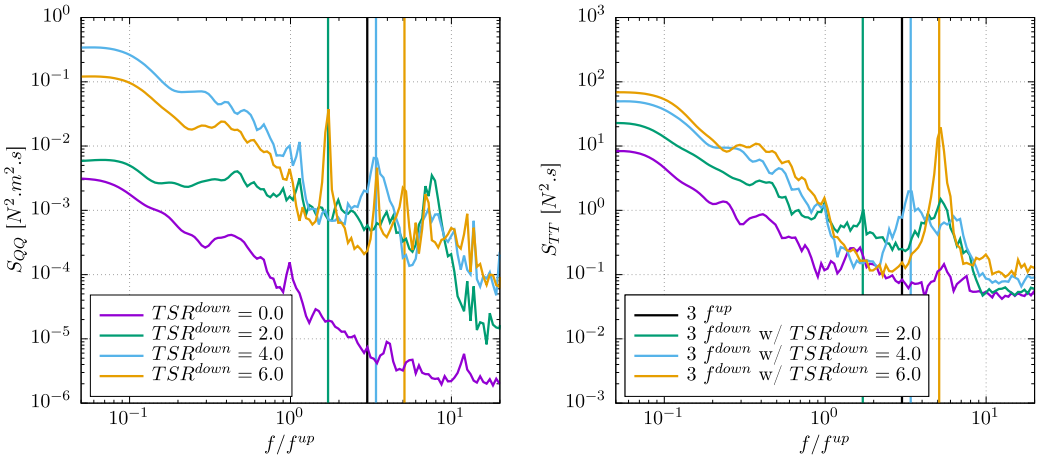

(a) S_{QQ} config. 1

(b) S_{TT} config. 1

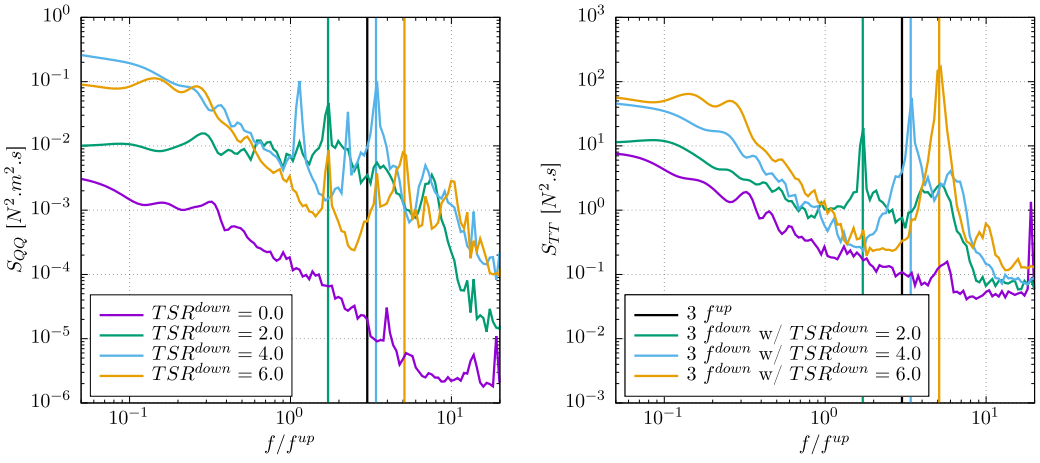

(c) S_{QQ} config. 2

(d) S_{TT} config. 2

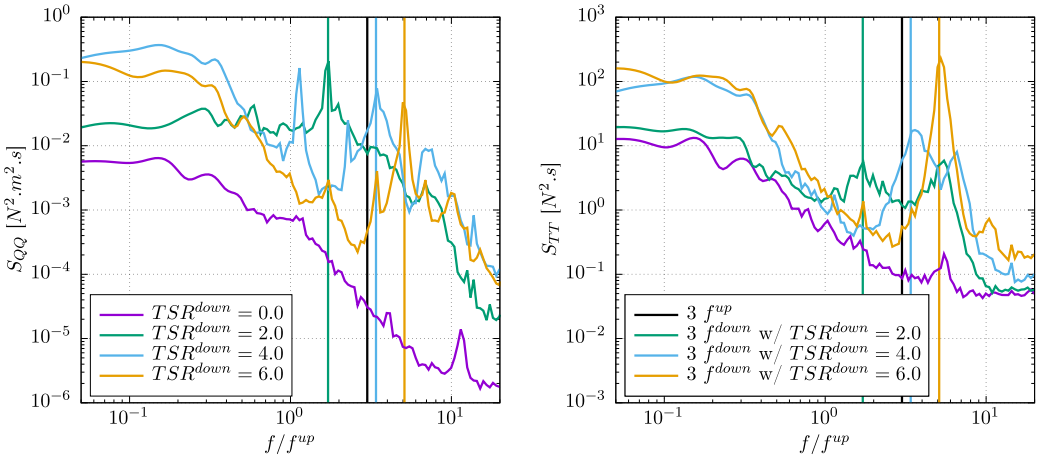

(e) S_{QQ} config. 3

(f) S_{TT} config. 3

Fig. 15. Power spectral density functions of the torque (S_{QQ}) and the thrust (S_{TT}) for selected *TSR*-values and the three configurations for the lowest turbulence rate.

very fast which would enable a higher density of turbines in a farm during a future real-size array development. For all the three cases, the downstream wake does not seem to be affected by the two upstream ones. All the downstream wakes show a more rapid lateral expansion than in the single turbine configuration at this given turbulence intensity. For configuration 3 only, the downstream wake presents a wake asymmetry. However, the major difference stands in the fact that the downstream wake generated turbulence is always higher than for the two upstream ones.

In terms of performance for the lowest turbulence rate, only the symmetric configuration presents a clear increase of downstream turbine performance with respect to the single turbine case. This was anticipated by the velocity increase in the bypass between the two upstream turbines. However, this improved power coefficient

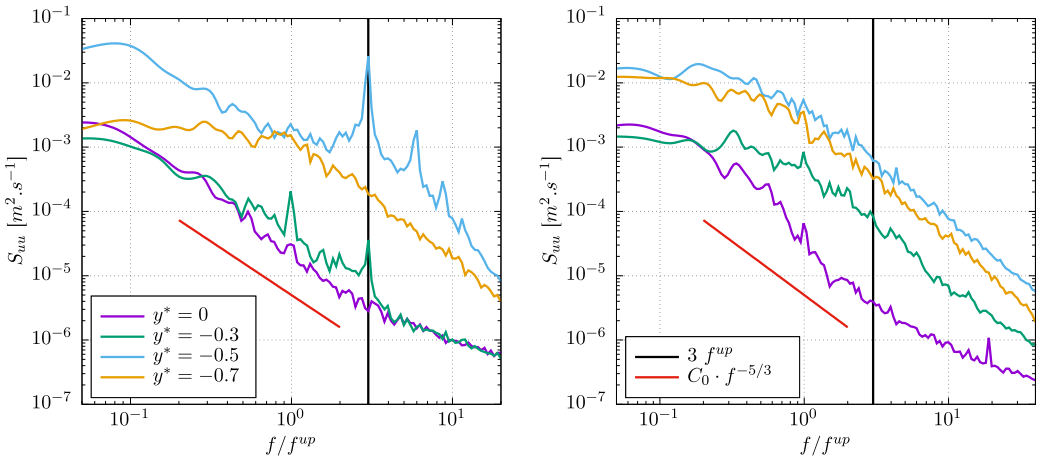

(a) S_{uu} for $x^* = 1.2$ (b) S_{uu} for $x^* = 3.0$

Fig. 16. Power spectral density functions of the velocity (S_{uu}) measured with LDV at $x^* = [1.2, 3.0]$ and $y^* = [0, -0.3, -0.5, -0.7]$, when $TSR^{up} = TSR^{down} = 3.5$ and for the lowest turbulence rate.

is only present at this low turbulence intensity and a quite large decrease of power performance is observed for the same configuration for the highest ambient turbulence intensity. To conclude on this, looking for improvement of turbine performance using this Venturi effect in the bypass for commercial farm configuration seems to be highly hypothetical. A small misalignment of the layout axis with respect to the tidal current may result in a decrease of performance at the end. In fact, both off-centred configurations for the lowest turbulence intensity either depict a similar behaviour or a decrease of performance with respect to the single turbine configuration. For the intermediate configuration, a quite similar power curve has been obtained. This is due to the fact that the velocity increase in the bypass counter balance the velocity deficit in the portion of the turbine submitted to the upstream wake. For the more off-centred configuration, a large power deficit is experimentally observed. For the highest ambient turbulence intensity, all downstream turbine power coefficients present a decrease with respect to the reference single configuration. The thrust coefficients are all affected but the modifications are not significant (generally an increase for the lower I_∞ and a decrease for the higher I_∞). However, it is the fluctuations of these C_P and C_T that are more largely impacted. To summarise, an increase is observed for both $\sigma(C_P)$ and $\sigma(C_T)$, the increase being the smaller for the symmetric configuration and gradually increasing for the more off-centred downstream turbine position. The $\sigma(C_T)$ increase can be up to approximately 7 times higher than the single reference case. And as expected from the wake measurements, these values of $\sigma(C_P)$ and $\sigma(C_T)$ are slightly increased for all the three configurations for the highest turbulence rate, but the three obtained curves have a similar trend.

Finally, one of the main objective of this study was to investigate the spectral signature of the upstream turbine (through its wake) in the downstream turbine performance. Unexpectedly, no upstream turbine frequency has been found in the spectral density functions of the downstream turbine parameters (torque or thrust), neither for the highest turbulence case nor for the lowest one, and whatever the configuration is. The absence of upstream turbine signature, even for more off-centred configuration with the lower ambient turbulence rate, has been noticed in the velocity spectral analysis as well, from 3 diameters distance. In fact, investigating load fluctuations, such as Ahmed et al. [40] or Togneri et al. [28,42], on the turbine in a farm may reveal easier (or perhaps less complicated) than expected.

Declaration of competing interest

The authors declare that they have no known competing financial interests or personal relationships that could have appeared to influence the work reported in this paper.

Acknowledgements

Authors would like to thank Normandy Regional Council and Ifremer for their joint effort in financing the PhD grant of Clément Carlier. This project was partly financially supported by the European Union (FEDER), the French government, IFREMER and the region Hauts-de-France in the framework of the project CPER 2015-2020 MARCO. Authors would like to thank the Normandy Regional Council and the European Union as well for their financial support in the framework of the NEPTUNE programme and the Normandy Regional funding SEMARIN and DIADEMAR. Authors are also most grateful to Thomas Bacchetti and Jean-Valery Facq for their help in the present work.

References

[1] P. Mycek, B. Gaurier, G. Germain, G. Pinon, E. Rivoalen, Experimental study of the turbulence intensity effects on marine current turbines behaviour. Part I: one single turbine, Renew. Energy 66 (2014) 729–746, https://doi.org/10.1016/j.renene.2013.12.036. URL, http://www.sciencedirect.com/science/article/pii/S096014811400007X.

[2] P. Mycek, B. Gaurier, G. Germain, G. Pinon, E. Rivoalen, Experimental study of the turbulence intensity effects on marine current turbines behaviour. Part II: two interacting turbines, Renew. Energy 68 (2014) 876–892, https://doi.org/10.1016/j.renene.2013.12.048. URL, http://www.sciencedirect.com/science/article/pii/S0960148114000196.

[3] R. Rawlinson-Smith, I. Bryden, M. Folley, V. Martin, T. Stallard, C. Stock-Williams, R. Willden, The PerAWaT project: performance assessment of wave and tidal array systems, in: 3rd International Conference on Ocean Energy, 2010.

[4] L.E. Myers, A.S. Bahaj, Experimental analysis of the flow field around horizontal axis tidal turbines by use of scale mesh disk rotor simulators, Ocean Eng. 37 (2) (2010) 218–227, https://doi.org/10.1016/j.oceaneng.2009.11.004. URL, http://www.sciencedirect.com/science/article/pii/S0029801809002613.

[5] L.E. Myers, A.S. Bahaj, An experimental investigation simulating flow effects in first generation marine current energy converter arrays, Renew. Energy 37 (1) (2012) 28–36, https://doi.org/10.1016/j.renene.2011.03.043. URL, http://www.sciencedirect.com/science/article/pii/S0960148111001716.

[6] P. Mycek, B. Gaurier, G. Germain, G. Pinon, E. Rivoalen, Numerical and

experimental study of the interaction between two marine current turbines, Int. J. Mar. Energy 1 (2013) 70–83, https://doi.org/10.1016/j.ijome.2013.05.007. URL, http://www.sciencedirect.com/science/article/pii/S2214166913000088.

[7] T. Stallard, R. Collings, T. Feng, J. Whelan, Interactions between tidal turbine wakes: experimental study of a group of three-bladed rotors, Philos. Trans. R. Soc. A Math. Phys. Eng. Sci. 371 (2013) 20120159, https://doi.org/10.1098/rsta.2012.0159.

[8] M. Nuernberg, L. Tao, Experimental study of wake characteristics in tidal turbine arrays, Renew. Energy 127 (2018) 168–181, https://doi.org/10.1016/j.renene.2018.04.053. URL, http://www.sciencedirect.com/science/article/pii/S0960148118304610.

[9] Y. Kervella, G. Germain, B. Gaurier, J.V. Facq, T. Bacchetti, Mise en évidence de l'importance de la turbulence ambiant sur les effets d'interaction entre hydroliennes, in: XIIIèmes Journées Nationales Génie Côtier - Génie Civil, 2014.

[10] M. J. Churchfield, L. Ye, P. J. Moriarty, A large-eddy simulation study of wake propagation and power production in an array of tidal-current turbines, Philos. Trans. R. Soc. A Math. Phys. Eng. Sci. 371. doi:10.1098/rsta.2012.0421.

[11] R. Malki, I. Masters, A.J. Williams, T.N. Croft, The influence on tidal stream turbine spacing on performance, in: 9th European Wave and Tidal Energy Conference, EWTEC), Southampton, UK, 2011.

[12] D.M. O'Doherty, A. Mason-Jones, C.E. Morris, T. O'Doherty, C. Byrne, B. B, P.W. Prickett, R.I. Grosvenor, Interaction of marine turbines in close proximity, in: 9th European Wave and Tidal Energy Conference, EWTEC), Southampton, UK, 2011.

[13] T. Blackmore, B. Gaurier, L. Myers, G. Germain, A.S. Bahaj, The effect of free-stream turbulence on tidal turbines, in: 11th European Wave and Tidal Energy Conference (EWTEC), Nantes, France, 2015.

[14] T. Blackmore, L.E. Myers, A.S. Bahaj, Effects of turbulence on tidal turbines: implications to performance, blade loads, and condition monitoring, Int. J. Mar. Energy 14 (2016) 1–26, https://doi.org/10.1016/j.ijome.2016.04.017. URL, http://www.sciencedirect.com/science/article/pii/S2214166916300297.

[15] T. Blackmore, W.M.J. Batten, A.S. Bahaj, Inlet grid-generated turbulence for large-eddy simulations, Int. J. Comput. Fluid Dyn. 27 (6–7) (2013) 307–315, https://doi.org/10.1080/10618562.2013.819972.

[16] O. Durán-Medina, F.G. Schmitt, R. Calif, G. Germain, B. Gaurier, Correlation between synchronised power and flow measurements, a way to characterize turbulence effects on marine current turbine, in: 11th European Wave and Tidal Energy Conference (EWTEC), Nantes, France, 2015.

[17] O. Durán-Medina, F.G. Schmitt, R. Calif, G. Germain, B. Gaurier, Turbulence analysis and multiscale correlations between synchronized flow velocity and marine turbine power production, Renew. Energy 112 (2017) 314–327, https://doi.org/10.1016/j.renene.2017.05.024. URL, http://www.sciencedirect.com/science/article/pii/S0960148117304093.

[18] C. Frost, I. Benson, P. Jeffcoate, B. Elsäßer, T. Whittaker, The effect of control strategy on tidal stream turbine performance in laboratory and field experiments, Energies, 11, 6, 10.3390/en11061533, URL, http://www.mdpi.com/1996-1073/11/6/1533.

[19] E. Osalusi, J. Side, R. Harris, Reynolds stress and turbulence estimates in bottom boundary layer of Fall of Warness, Int. Commun. Heat Mass Transf. 36 (5) (2009) 412–421, https://doi.org/10.1016/j.icheatmasstransfer.2009.02.004. URL, http://www.sciencedirect.com/science/article/pii/S073519330900044X.

[20] E. Osalusi, J. Side, R. Harris, Structure of turbulent flow in EMEC's tidal energy test site, Int. Commun. Heat Mass Transf. 36 (5) (2009) 422–431, https://doi.org/10.1016/j.icheatmasstransfer.2009.02.010. URL, http://www.sciencedirect.com/science/article/pii/S0735193309000530.

[21] I.A. Milne, R.N. Sharma, R.G.J. Flay, S. Bickerton, Characteristics of the turbulence in the flow at a tidal stream power site, Philos. Trans. R. Soc. A Math. Phys. Eng. Sci. 371 (2013), https://doi.org/10.1098/rsta.2012.0196.

[22] J. Thomson, B. Polagye, V. Durgesh, M.C. Richmond, Measurements of turbulence at two tidal energy sites in puget sound, wa, IEEE J. Ocean. Eng. 37 (3) (2012) 363–374, https://doi.org/10.1109/JOE.2012.2191656.

[23] J. MacEnri, M. Reed, T. T., Influence of tidal parameters on SeaGen flicker performance, Philos. Trans. R. Soc. A Math. Phys. Eng. Sci. 371. doi:10.1098/rsta.2012.0247.

[24] Y. Li, J.A. Colby, N. Kelley, R. Thresher, B. Jonkman, S. Hughes, Inflow measurement in a tidal strait for deploying tidal current turbines: lessons, opportunities and challenges, in: 29th International Conference on Ocean, Offshore and Arctic Engineering, vol 3, 2010, pp. 569–576, https://doi.org/10.1115/OMAE2010-20911.

[25] V.S. Neary, B. Gunawan, D.C. Sale, Turbulent inflow characteristics for hydrokinetic energy conversion in rivers, Renew. Sustain. Energy Rev. 26 (2013) 437–445, https://doi.org/10.1016/j.rser.2013.05.033. URL, http://www.sciencedirect.com/science/article/pii/S1364032113003365.

[26] B. Gunawan, V.S. Neary, J. Colby, Tidal energy site resource assessment in the East River tidal strait, near Roosevelt Island, New York, New York, Renew. Energy 71 (2014) 509–517, https://doi.org/10.1016/j.renene.2014.06.002. URL, http://www.sciencedirect.com/science/article/pii/S0960148114003425.

[27] J. McMillan, A. Hay, R. Lueck, F. Wolk, An assessment of the TKE balance at a tidal energy site using ADCP and shear probe measurements, in: 12th European Wave and Tidal Energy Conference (EWTEC), Cork, Ireland, 2017.

[28] M. Togneri, I. Masters, C. Carlier, C. Choma Bex, G. Pinon, Comparison of synthetic turbulence approaches for two numerical tidal turbine models, in: 12th European Wave and Tidal Energy Conference, Cork, Ireland, 2017.

[29] B. Gaurier, G. Germain, J.-V. Facq, T. Bacchetti, Wave and current flume tank of Ifremer at Boulogne-sur-mer. Description of the facility and its equipment, Tech. Rep. (2018), https://doi.org/10.13155/58163. URL, https://archimer.ifremer.fr/doc/00470/58163/.

[30] F. Maganga, G. Germain, J. King, G. Pinon, E. Rivoalen, Experimental characterisation of flow effects on marine current turbine behaviour and on its wake properties 4 (6) (2010) 498–509, https://doi.org/10.1049/iet-rpg.2009.0205.

[31] B. Gaurier, G. Germain, G. Pinon, How to correctly measure turbulent upstream flow for marine current turbine performance evaluation?, in: Proceedings of the 3rd International Conference on Renewable Energies Offshore, Lisbon, Portugal, 2018. URL, http://www.centec.tecnico.ulisboa.pt/renew2018/.

[32] B. Gaurier, G. Germain, J.-V. Facq, T. Bacchetti, C. Carlier, G. Pinon, Three Tidal Turbines in Interaction: an Experimental Data-Set on Wake and Performances, 2018, https://doi.org/10.17882/58149. URL, https://www.seanoe.org/data/00470/58149/.

[33] J.I. Whelan, J.M.R. Garaham, J. Peiró, A free-surface and blockage correction for tidal turbines, J. Fluid Mech. 624 (2009) 281–291, https://doi.org/10.1017/S0022112009005916.

[34] B. Gaurier, G. Germain, J.-V. Facq, C.M. Johnstone, A.D. Grant, A.H. Day, E. Nixon, F. Di Felice, M. Costanzo, Tidal energy "Round Robin" tests comparisons between towing tank and circulating tank results, special Issue on Marine Renewables Infrastructure Network, Int. J. Mar. Energy 12 (2015) 87–109, https://doi.org/10.1016/j.ijome.2015.05.005. URL, http://www.sciencedirect.com/science/article/pii/S2214166915000223.

[35] A.S. Bahaj, A.F. Molland, J.R. Chaplin, W.M.J. Batten, Power and thrust measurements of marine current turbines under various hydrodynamic flow conditions in a cavitation tunnel and a towing tank, Renew. Energy 32 (3) (2007) 407–426, https://doi.org/10.1016/j.renene.2006.01.012. URL, http://www.sciencedirect.com/science/article/pii/S0960148106000516.

[36] G. Pinon, M.F. Hurst, E. Lukeba, Semi-analytical estimate of energy production from a tidal turbine farm with the account of ambient turbulence, Int. J. Mar. Energy 19 (2017) 70–82, https://doi.org/10.1016/j.ijome.2017.05.003. URL, http://www.sciencedirect.com/science/article/pii/S2214166917300516.

[37] V. Cognet, S. Courrech du Pont, I. Dobrev, F. Massouh, B. Thiria, Bioinspired turbine blades offer new perspectives for wind energy, Proc. R. Soc. A Math. Phys. Eng. Sci. 473 (2017), https://doi.org/10.1098/rspa.2016.0726.

[38] R. Martinez, G.S. Payne, T. Bruce, The effects of oblique waves and currents on the loadings and performance of tidal turbines, Ocean Eng. 164 (2018) 55–64, https://doi.org/10.1016/j.oceaneng.2018.05.057. URL, http://www.sciencedirect.com/science/article/pii/S0029801818309296.

[39] P. Mycek, G. Pinon, C. Lothodé, A. Dezotti, C. Carlier, Iterative solver approach for turbine interactions: application to wind or marine current turbine farms, Appl. Math. Model. 41 (2017) 331–349, https://doi.org/10.1016/j.apm.2016.08.027. URL, http://www.sciencedirect.com/science/article/pii/S0307904X16304516.

[40] U. Ahmed, D.D. Apsley, I. Afgan, T. Stallard, P.K. Stansby, Fluctuating loads on a tidal turbine due to velocity shear and turbulence: comparison of CFD with field data, Renew. Energy 112 (2017) 235–246, https://doi.org/10.1016/j.renene.2017.05.048. URL, http://www.sciencedirect.com/science/article/pii/S0960148117304330.

[41] M. Togneri, M. Lewis, S. Neill, I. Masters, Comparison of ADCP observations and 3D model simulations of turbulence at a tidal energy site, Renewable Energy 114 (2017) 273–282, https://doi.org/10.1016/j.renene.2017.03.061.

[42] M. Togneri, G. Pinon, C. Carlier, C. Choma Bex, I. Masters, Comparison of synthetic turbulence approaches for blade element momentum theory prediction of tidal turbine performance and loads, Renewable Energy 145 (2020) 408–418, https://doi.org/10.1016/j.renene.2019.05.110.